Nanoscale Advances

ROYAL SOCIETY OF CHEMISTRY

PAPER

View Article Online
View Journal

Cite this: DOI: 10.1039/d6na00256k

CO_2 electroreduction on nano-Cu-ZIF grown inside activated carbon: experimental and computational aspects

Santanu Jana, †[a] Gaurav Mukherjee,†[a] Asmita Dutta,[a] Hani Porat,[a] Aneena Lal, [ab] Alon Khabra,[a] Itay Pitussi[a] and Arie Borenstein *[a]

Electrochemical reduction of CO_2 (CO_2RR) offers a sustainable approach to simultaneously lower atmospheric CO_2 levels and convert it into useful chemicals. While noble metals are currently the most effective catalysts for this process, their expense limits large-scale use, driving the search for more affordable alternatives. Transition-metal sites incorporated within metal–organic frameworks (MOFs) show great catalytic promise; however, the inherently poor conductivity of MOFs remains a significant obstacle. The porous structure of activated carbon provides a high surface area for efficient electron transport and CO_2 adsorption, while the encapsulated MOF imparts catalytic sites with tuneable electronic properties and molecular selectivity. The synergistic interaction between the MOF and AC enhances the availability of active sites, conductivity, improves charge transfer kinetics, and suppresses competing hydrogen evolution. In this work, Cu-Zeolitic Imidazole Framework (Cu-ZIF) nanoparticles were grown directly within a hierarchically porous activated carbon matrix, rather than physically blended with conductive additives. This encapsulation strategy resulted in composites with enhanced conductivity, maintained Cu-ZIF crystallinity, and strong electronic coupling between the components. When applied to electrochemical CO_2RR, the Cu-ZIF@AC composite achieved low overpotential of −0.56 V (*vs.* RHE) at −10 mA cm^{-2} current density, surpassing the performance of usually reported MOF-based systems. Moreover, the catalyst selectively produced acetic acid (71.5% faradaic efficiency) at −0.3 V (*vs.* RHE) onset potential demonstrating excellent potential for efficient and scalable CO_2 electroreduction.

Received 1st April 2026
Accepted 29th May 2026

DOI: 10.1039/d6na00256k

rsc.li/nanoscale-advances

1 Introduction

The escalating concentration of atmospheric CO_2, primarily from the continuous burning of fossil fuels, poses a severe environmental threat by exacerbating climate change.[1] Long-term atmospheric monitoring indicates that the global mean CO_2 concentration has increased by approximately 35% over the past six decades, as evidenced by continuous records such as the Keeling curve.[2] Addressing this global challenge requires developing sustainable solutions for CO_2 utilization. Among the various CO_2 conversion methods, the electrochemical carbon dioxide reduction reaction (CO_2RR) has garnered significant interest as an economically viable approach to transform CO_2 into valuable chemicals and fuels.[3,4]

Despite its promise, CO_2RR faces significant hurdles. A major challenge is the requirement for high overpotentials to activate the stable CO_2 molecule. Furthermore, CO_2RR in aqueous solutions is highly competitive with the hydrogen evolution reaction (HER), as their redox potentials are close.[5–8] This competition necessitates the use of catalysts with high selectivity to ensure the CO_2RR is efficient and prevents energy waste on HER.

Copper (Cu) stands out among transition metals as effective catalyst for highly reduced products like hydrocarbons and alcohols from CO_2, rather than just CO.[9] This is attributed to Cu's ability to facilitate C–C bond formation and reduce the energy needed for CO binding. However, Cu catalysts typically suffer from low faradaic efficiency (F.E.) and selectivity toward a single product due to the competitive HER and numerous potential-dependent reaction pathways.[10–12] Overcoming these limitations often involves controlling catalyst morphology, support materials, and electrolyte conditions.

Recent studies have highlighted that the catalytic behaviour of Cu-based electrocatalysts during CO_2 electroreduction is strongly influenced not only by catalyst morphology and grain boundaries, but also by dynamic surface species formed under reaction conditions. For example, oxygen-containing adsorbates such as hydroxyl species were reported to strongly interact with Cu surfaces, influencing intermediate adsorption and

[a]*Department of Chemical Sciences, Ariel University, Ariel, Israel. E-mail: arieb@ariel.ac.il*

[b]*Institute of Chemistry, The Hebrew University of Jerusalem, Jerusalem, Israel*

† Equally contributing authors.

multicarbon product formation.[13] In addition, carbon deposition formed during CO_2 reduction has been identified as a critical deactivation pathway for Cu electrodes, particularly under methane-forming conditions, where deposited carbon blocks active sites and deteriorates catalytic stability.[14] Furthermore, defect-rich Cu catalysts containing abundant grain boundaries were shown to promote CO–CO coupling and enhance C_{2+} product selectivity by stabilizing key reaction intermediates.[15] These findings collectively demonstrate that catalyst reconstruction, surface poisoning, and interfacial adsorption phenomena play decisive roles in determining the activity, selectivity, and stability of Cu-based CO_2RR catalysts.

Metal–Organic Frameworks (MOFs), such as Zeolitic Imidazolate Framework-8 (ZIF-8), offer significant advantages for electrocatalysis, including atomically dispersed metal sites, tuneable porosity, large surface area, and high stability. MOFs possess three distinguishable sites—the metal node, the organic linker, and the pore space—where catalytic functions can be allocated.[12,16,17] These structural properties can potentially enhance catalytic performance,[18] leading to smaller onset potentials[19] and improved faradaic efficiency (F.E.).[20] Despite these benefits, MOFs inherently suffer from low electrical conductivity, which is a significant bottleneck for efficient charge transfer in electrocatalytic systems.[21] While pyrolyzing MOFs is one strategy to create a conductive carbon lattice with embedded metal atoms, this process typically destroys the unique electronic structure that supports the material's catalytic capacity, diminishing the MOF's advantages. Thus, there is an urgent need to engineer composite materials that combine the catalytic activity and product specificity of Cu with the high surface area and structural tunability of MOFs, while simultaneously addressing the conductivity issue.[22,23]

In this work, we report the *in situ* growth of Cu-Zeolitic Imidazole Framework (Cu-ZIF) within the porous architecture of activated carbon (AC) to obtain a highly conductive and structurally stable catalyst for electrochemical CO_2 reduction. The carbon scaffold facilitates efficient electron transport and improves the mechanical integrity of the Cu-ZIF domains under electrochemical operation. Importantly, Cu-ZIF MOF has not been previously investigated for CO_2 reduction, and the Cu-ZIF@AC composite introduced here represents a novel catalyst platform that integrates enhanced conductivity, improved stability, and accessible Cu active sites. This composite further promotes the efficient electroreduction of CO_2 toward a valuable carbon-based product.

2 Experimental section

2.1 Materials and reagents

Copper(II) nitrate trihydrate (Sigma-Aldrich, 99%), 2-methyl imidazole (2-MI) (SRL, 99%), potassium bicarbonate (SRL, 99%), sodium sulphate (CARLO ERBA Reagents, 99%).

2.2 Synthesis of Cu-ZIF

Copper(II) nitrate trihydrate was added to the 10 ml DI water in a beaker and stirred for 10 min. 2-Methyl imidazole (2-MI) was added to the 5 ml DI water in a beaker and stirred for 10 min. Copper(II) nitrate trihydrate and 2-methyl imidazole (2-MI) was taken in 1 : 2 mmol ratio. Then the 2-MI solution was added to the copper nitrate solution dropwise during stirring and kept the whole solution in stirring for few hours. Then the solution was transferred to a Teflon-lined stainless-steel autoclave and heated at 180 °C for 24 h. The obtained dark brown coloured ppt was washed with DI water followed by acetone and dried in an oven at 70 °C overnight. Then the powder was calcined at 150 °C for 4 h at rate of 1 °C min^{-1} in a tubular furnace.[24–26]

2.3 Synthesis of Cu-ZIF@AC

250 mg of activated carbon and copper(II) nitrate trihydrate was dispersed in 10 ml of DI water overnight. Then, 5 ml DI water solution of 2-methyl imidazole (2-MI) was added dropwise to the above solution followed by stirring. The metal precursor and organic linker was taken in 1 : 2 mmol ratio to get ultimate 7 wt% Cu-ZIF loading within the AC matrix. Next, the solution was transferred in a Teflon lined stainless steel autoclave and heated at 180 °C. After that, the obtained solid ppt was washed with DI water and acetone followed by centrifugation and dried. Then, the black powder obtained was calcined in tubular furnace at 150 °C for 4 h at a ramp rate of 1 °C min^{-1}.[25,27,28]

2.4 Instrumentations

Synthesized Cu-ZIF, Cu-ZIF@AC were calcined in KSL-1100X furnace equipped with quartz tube. The Powder X-ray Diffraction (PXRD) patterns of all the materials were analysed using X'Pert Pro X-ray diffractometer with Cu Kα radiation ($\lambda = 0.154$ nm). SEM images were taken by High Resolution Scanning Electron Microscope (HRSEM, TESCAN MAIA3). The pore distribution and surface area of the samples were analysed using the Micrometric TriStar 11PLUS. Thermogravimetric analysis was performed using METTLER TOLEDO TGA/DSC 1 STAR^e system. The Raman spectroscopy of all the samples were performed using a confocal Raman microscope Alpha 300R, WItec, Germany with a 532 nm excitation wavelength at a laser power of 5 mW. All the electrochemical measurements were performed using BioLogic SP-150e potentiostat. The H_2 gas evolved during CO_2RR was measured using PFRIFFER VACUUM ^{Hi}CUBE Mass spectrometer. Fourier Transform Infrared (FTIR) spectroscopy of the samples was analysed using JASCO FT/IR-4700 spectrometer. The CO_2RR products were detected and quantified using BRUKER 400 MHz Nuclear Magnetic Resonance (NMR) Spectrometer.

2.5 Electrode fabrication

A catalyst ink was prepared by mixing active materials, 10% carbon black and 5% PTFE as binder followed by dispersing the mixture in isopropanol under stirring to form a homogeneous slurry. Then, 50 μL of the ink containing 3 mg of mass loading was drop-cast onto a 1 × 1 cm precleaned carbon paper. The coated carbon paper was dried at 60 °C to evaporate the solvent completely.

2.6 Electrochemical measurements

The electrochemical measurements were performed using a three-electrode setup in a H-type electrochemical cell having Nafion-117 separator between cathode and anode compartment. All the electrochemical studies were done in Biologic SP 150e electrochemical workstation. The working electrode was 1 × 1 cm carbon paper coated with the catalyst ink, coiled Pt wire served as counter electrode and Ag/AgCl (3 M KCl) electrode was used as reference electrode. All the measured potentials were converted to Reversible Hydrogen Electrode (RHE) value as following,[29]

$$E_{RHE} = E_{Ag/AgCl} + 0.0591 \times pH + E^{0}_{Ag/AgCl} \quad (1)$$

where, E_{RHE} is the potential *vs.* RHE; $E_{Ag/AgCl}$ is the potential applied *vs.* Ag/AgCl reference electrode, $E^{0}_{Ag/AgCl}$ is the standard potential of Ag/AgCl reference electrode.

The Cyclic Voltammetry (CV) of Cu-ZIF and Cu-ZIF@AC was done using 0.5 M Na_2SO_4. For analysing CO_2 reduction (CO_2RR) activity for Cu-ZIF@AC, the Linear Sweep Voltammetry (LSV) was performed in N_2 saturated 0.5 M Na_2SO_4 and CO_2 saturated 0.5 M $KHCO_3$. The gases were purged for 20 minutes for saturation. The comparative CV, LSVs of the materials were performed in CO_2 saturated 0.5 M $KHCO_3$. The stability of the catalyst was analysed using 12 h chronoamperometry at −0.56 V (*vs.* RHE) in CO_2 saturated 0.5 M $KHCO_3$.

2.7 Product quantification

400 MHz Nuclear Magnetic Resonance (NMR) was used for the detection and quantification of the CO_2 reduction products. The liquid products are collected from the electrochemical cell after chronoamperometry measurements at different potentials, *i.e.* −0.3, −0.4, −0.5, −0.56, −0.6, −0.7 V (*vs.* RHE). In all the samples acetic acid is the major products, formic acid and methanol are the minor products.

$$2CO_2 + 8H^+ + 8e^- \rightarrow CH_3COOH + 2H_2O \quad (2)$$

$$CO_2 + 2H^+ + 2e^- \rightarrow HCOOH \quad (3)$$

$$CO_2 + 6H^+ + 6e^- \rightarrow CH_3OH + H_2O \quad (4)$$

The products were quantified by collecting the electrolyte after chronoamperometry at different potentials and mixing it with 0.01 M maleic acid as an internal standard and 10% D_2O. The following equation was used to quantify the products,[30]

$$C_j = \frac{v_i \times \rho_i}{M_i} \times \frac{S_l}{S_i} \times \frac{m_i}{m_l} \times \frac{1}{v_e} \quad (5)$$

where, C_j is the concentration of the product, v_e is the volume of electrolyte collected; $\frac{S_l}{S_i}$ is the ratio of the area of the peaks of liquid product to the internal standard; v_i is the volume of internal standard added; M_i is the molecular weight of the internal standard; ρ_i is the density of the internal standard; $\frac{m_i}{m_l}$ is the ratio of the number of protons of internal standard to the liquid product.

For the competitive Hydrogen evolution reaction (HER), the H_2 was quantified using Mass Spectroscopy (MS).

Faradaic efficiency (F.E.) of each CO_2 reduction product was calculated to quantify the fraction of the total charge that directly contributed to the formation of that product. The F.E. is determined according to,[27]

$$F.E.(\%) = \frac{nFz}{It} \times 100 \quad (6)$$

where, n is the number moles of the product; F is the Faraday constant (96 485 C mol^{-1}); z is the number electrons required for a particular product formation as shown in the reactions (2–4);[31] I is the current applied, t is the duration of the electrocatalysis.

2.8 Computational details

Spin-polarized density functional theory (DFT) calculations were carried out using periodic boundary conditions in the Vienna *Ab initio* Simulation Package (VASP)[32] to investigate the Cu-ZIF's structural features, CO_2 adsorption behaviour, and catalytic mechanisms. The exchange–correlation energy was described using the generalized gradient approximation (GGA) with the Perdew–Burke–Ernzerhof (PBE) functional.[33,34] Electron-ion interactions were taken into consideration using the projector-augmented wave (PAW) method.[35] Grimme's D3 dispersion correction (PBE-D3) was implemented to account for van der Waals interactions.[36] All atoms were completely relaxed until the total energy and atomic forces converged to less than 10^{-6} eV and 2 × 10^{-2} eV $Å^{-1}$, respectively, using a plane-wave cutoff energy of 500 eV. Due to the large size of the ZIF unit cell, a 1 × 1 × 1 Monkhorst–Pack k-point grid was used for Brillouin-zone sampling.[37]

The zero-point energy (ZPE) and entropy contribution were included in all Gibbs free energy calculations. The ZPE was evaluated using a second-order finite-difference method based on the numerical differentiation of forces with a step size of 0.015 Å and computed at room temperature using VASPKIT.[38] In this study, the adsorption energy (E_{ads}) was calculated according to the following eqn (7):[39]

$$E_{ads} = E_{*CO_2} - (E_* + E_{CO_2}) \quad (7)$$

where E_{*CO_2}, E_*, and E_{CO_2} represent the free energies of the adsorbed system, the isolated Cu-ZIF, and the CO_2 molecule, respectively.

The energy of the reaction is defined as the difference in the energies of the product(s) and reactant(s) as shown in eqn (8):[40]

$$E_{rxn} = \sum E_{product} - \sum E_{reactant} \quad (8)$$

where E_{rxn}, $E_{product}$, $E_{reactant}$ represents the total energy of the reaction, total energy of the products and total energy of the reactant respectively.

To account for the influence of the applied electrochemical potential on the free energies of adsorbed intermediates, the computational hydrogen electrode (CHE) framework introduced by Nørskov and co-workers is adopted. Within this

approach, all thermodynamic quantities are referenced to the reversible hydrogen electrode (RHE).[41,42] The reaction free energy at a given potential U is therefore obtained from eqn (9).

$$\Delta E_{\text{reaction}}(U) = \Delta E_{\text{reaction}}(0) - neU \quad (9)$$

where n denotes the number of electrons transferred in the elementary step (here, $n = 1$ for each redox step), e is the elementary charge, and U is the applied electrode potential. Consequently, elementary steps involving coupled proton–electron transfer exhibit a linear dependence on the applied potential, whereas non-redox transformations such as C–O bond cleavage remain unaffected by changes in U. Throughout this work, all free-energy evaluations are carried out at pH = 0, consistent with standard CHE conventions.

2.9 Structural optimization

In this study, we optimized the structure of Cu-ZIF for the first time. The Cu-ZIF structure was adopted from the ZIF-8 MOF[43] (Fig. S9) which contained 96 carbon, 120 hydrogen, 48 nitrogen and 12 zinc atoms. The ZIF-8 was modified by substituting 12 Zn atoms with Cu atoms to form Cu-ZIF. Each Cu atoms are bonded with the N-sites of 2-methyl imidazole (2-MI) organic molecules forming an elipto-spherical structure. Each unit cell of the Cu-ZIF was formed by the complexation of 12 Cu $(C_4H_5N_2 = \text{2-MI})_2$ units in which the bi-coordinated copper metal atoms coordinated with the chelating nitrogen sites of the other 2-methyl imidazole units, hence forming the bulk Cu-ZIF.

3 Results and discussions

To explain the advantages of MOF-encapsulated activated carbon, we have grown Cu-ZIF MOF inside the pores of activated carbon. The Cu-ZIF@AC composite was prepared as follows. First, copper nitrate trihydrate and Activated Carbon (AC) were dispersed overnight under stirring in an aqueous solution. Next, the 2-MI solution was added dropwise for a few hours, followed by a hydrothermal reaction, as illustrated in Fig. 1.

3.1 Physical characterization

The crystal structure of the Cu-ZIF, Cu-ZIF@AC, and AC were characterized using a Powder X-ray Diffractometer (PXRD) with Cu Kα radiation (λ = 0.154 nm). The XRD pattern of the Cu-ZIF@AC composite perfectly matched the PXRD peaks of Cu-ZIF, having 2θ values at 14.46°, 29.62°, 31.52°, 33.1°, 34.85°, 39.54°, 44.88°, and 48.01°, indicating the successful formation of Cu-ZIF inside the activated carbon pores.[24,26] The peak at 14.46° 2θ value for Cu-ZIF@Ac is sharper than Cu-ZIF indicates the increase in crystallinity due to the growth of nano-Cu-ZIF inside activated carbon pores. In addition, a peak is observed at a 2θ° value of 26.35° corresponding to the (002) planes of graphitic segments of activated carbon (AC), as shown in Fig. 2a. Virtually all the MOF particles were confined within the carbon pores, as evidenced by the HRSEM images (Fig. S1). EDS elemental mapping of copper was performed to provide direct evidence for the encapsulation and spatial distribution of Cu-MOF within the activated carbon. As shown in Fig. S2, the Cu elemental signal is uniformly distributed throughout the activated carbon without the presence of localized Cu-rich regions or phase separation. The homogeneous dispersion of Cu confirms the successful encapsulation of copper species.

The bonding property was characterized using a Fourier Transform Infrared Spectrometer (FTIR). The FTIR spectrum (Fig. 2b) of Cu-ZIF displays the characteristic vibrational bands corresponding to the 2-methyl imidazole linker, including C–N, C=N, and C–H modes, along with the Cu–N band, confirming the integrity of the framework.[24,26] In the Cu-ZIF@AC composite, these bands are significantly suppressed due to the dominant absorption features of activated carbon, which mainly show C=C stretching and a broad O–H band. The overlap and reduced intensity of Cu-ZIF signals in the composite reconfirm the successful encapsulation of Cu-ZIF inside the pores of activated carbon.

The Raman spectrum (Fig. 2c) of pristine Cu-ZIF exhibits distinct Cu–N vibrational modes in the low-frequency region (280 cm^{-1}) reflecting the preserved metal–ligand coordination environment.[26] In the Cu-ZIF@AC composite, these Cu–N features are largely suppressed due to the dominant carbonaceous scattering originating from activated carbon. The pronounced D and G bands in both AC and Cu-ZIF@AC further confirm the incorporation of Cu-ZIF mainly inside the pores of activated carbon.

The thermal stability was measured using thermal gravimetry analysis (TGA). The TGA profiles (Fig. 2d) show that the pristine Cu-ZIF undergoes substantial mass loss at ~180 °C and ~325 °C, while the Cu-ZIF@AC composite displays a gradual degradation pattern, indicating improved thermal stability.[24,26]

Determining the surface area of porous materials is crucial for understanding their catalytic performance. N_2 gas adsorption–desorption was performed for all the materials at 77 K for

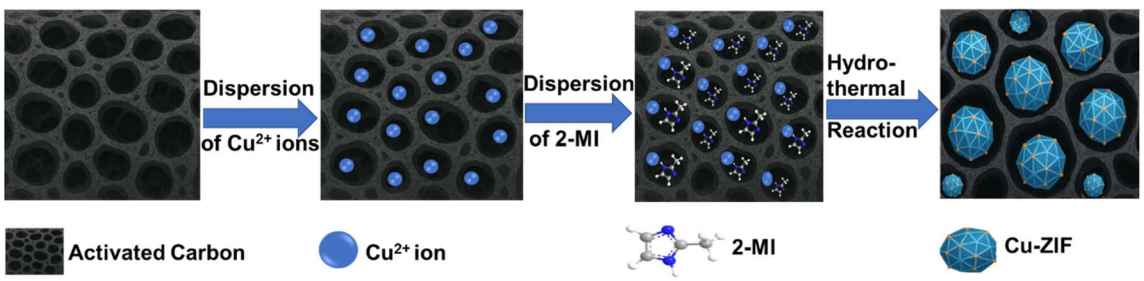

Fig. 1 Schematic diagram of the synthetic process of MOF encapsulated activated carbon.

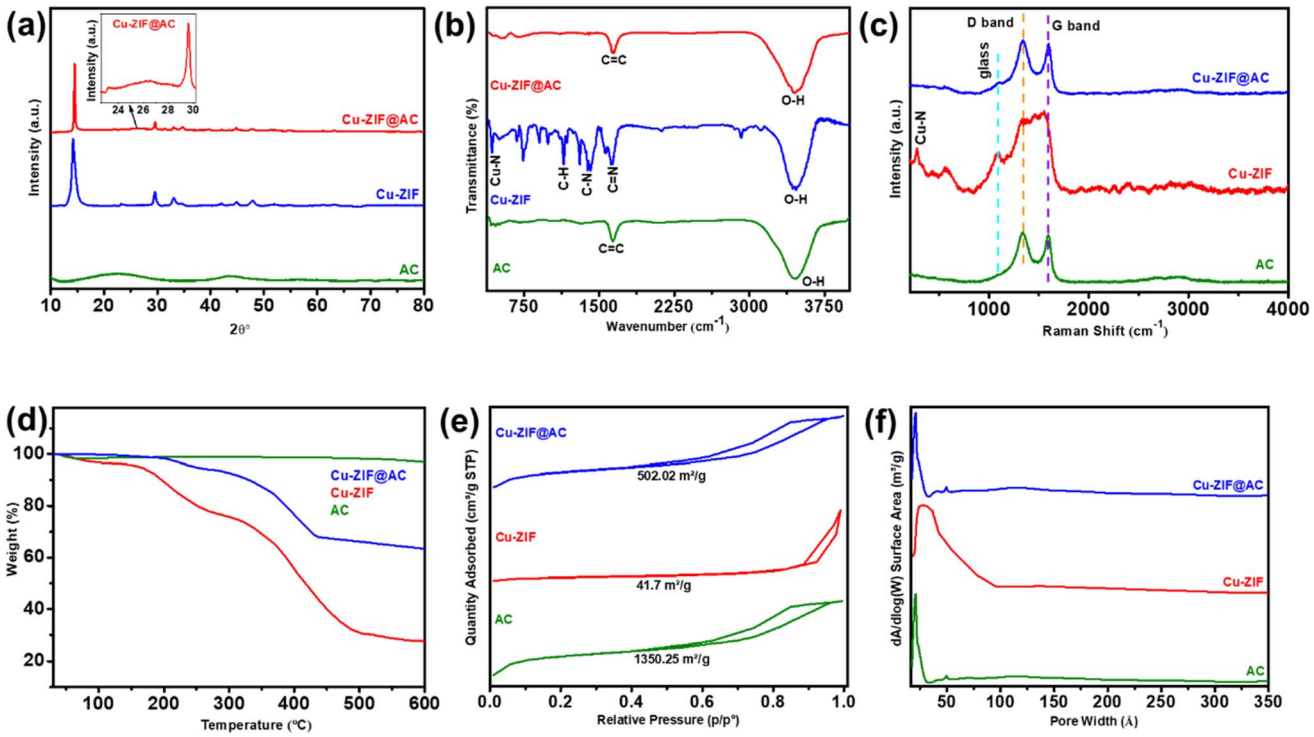

Fig. 2 (a) XRD pattern of AC, Cu-ZIF, Cu-ZIF@AC where to the (002) planes of week graphitic segments of Activated Carbon (AC) as shown in the projected view; (b) FTIR spectrum of AC, Cu-ZIF, Cu-ZIF@AC showing the vibrational modes; (c) Raman spectra of AC, Cu-ZIF, Cu-ZIF@AC powders coated on glass slide (d) TGA diagram of AC, Cu-ZIF, Cu-ZIF@AC for thermal stability test; (e) N_2 gas adsorption isotherms of AC, Cu-ZIF, Cu-ZIF@AC mentioning the surface areas; (f) BJH model for pore distribution of AC, Cu-ZIF, Cu-ZIF@AC based on N_2 gas adsorption experiment.

the estimation of surface area and porosity. The N_2 adsorption–desorption isotherm (Fig. 2e) of Cu-ZIF@AC exhibits combined Type I(b)/Type IV(a) characteristics, indicating hierarchical porosity generated when Cu-ZIF nanocrystals grow inside the activated-carbon framework.[44–46] The strong uptake at low P/P_0 corresponds to the preserved micro-porosity of AC (1350.25 m^2 g^{-1}), while the additional rise at intermediate pressures reflects the formation of new mesopores during MOF nucleation within the carbon pores. This is further supported by the H4 hysteresis loop, typical of slit-shaped micro–mesoporous structures derived from the AC scaffold. In contrast, pristine Cu-ZIF shows a weak Type IV(a) isotherm with an H3 hysteresis and a very low surface area (41.7 m^2 g^{-1}).[44–46] The significant decrease in BET surface area for Cu-ZIF@AC (502.02 m^2 g^{-1}) compared to AC confirms that the MOF growth is confined within the carbon matrix, resulting in a more interconnected and accessible pore network.

The pore-size distribution curves (Fig. 2f) show clear differences in the porous structures of the three materials. AC exhibits a strong peak at ~20 Å, confirming its predominantly microporous character with narrow slit-shaped mesopores.[44–46] Pristine Cu-ZIF displays a broad distribution centred at ~30 Å, arising from mesopores.[44–46] In the Cu-ZIF@AC composite, the distribution is dominated by the AC-derived micropores, while the broad mesopore peak of Cu-ZIF is largely suppressed. This indicates that Cu-ZIF nucleates within the confined carbon pores, thereby limiting the formation of large mesopores. Inductively Coupled Plasma Optical Spectroscopy (ICP-OES) quantified the copper (Cu) content of the Cu-ZIF@AC composite as 2.1 wt% (Table 1).

3.2 Electrochemical tests

The Cu-ZIF@AC was investigated as a cathode in an electrocatalysis system. To prepare the electrodes, an ink comprising active materials, carbon black as a conductive agent, and PTFE as a binder was prepared and drop-cast onto carbon paper. To evaluate the electrochemical profiles, cyclic voltammetry (CV) was performed at 50 mV s^{-1} scan rate for all materials in a N_2-saturated 0.5 M Na_2SO_4 solution. The Cu-ZIF@AC showed Cu^+/Cu^{2+} redox couple at 1.28 and 0.2 V *vs.* RHE, whereas the Cu-ZIF showed Cu^+/Cu^{2+} redox couple at 1.01 and 0.57 V *vs.* RHE (Fig. 3a). The area under the CV curve of Cu-ZIF@AC is larger than that of pristine Cu-ZIF, indicating a higher electrical conductivity of the composite compared to the MOF.

To directly verify the improved conductivity of the composite, Electrochemical Impedance Spectroscopy (EIS)

Table 1 The wt% of Cu in the composite Cu-ZIF@AC determined using ICP-OES

Sample	Wt% of Cu determined by ICP-OES
Cu-ZIF@AC	2.1 ± 0.002

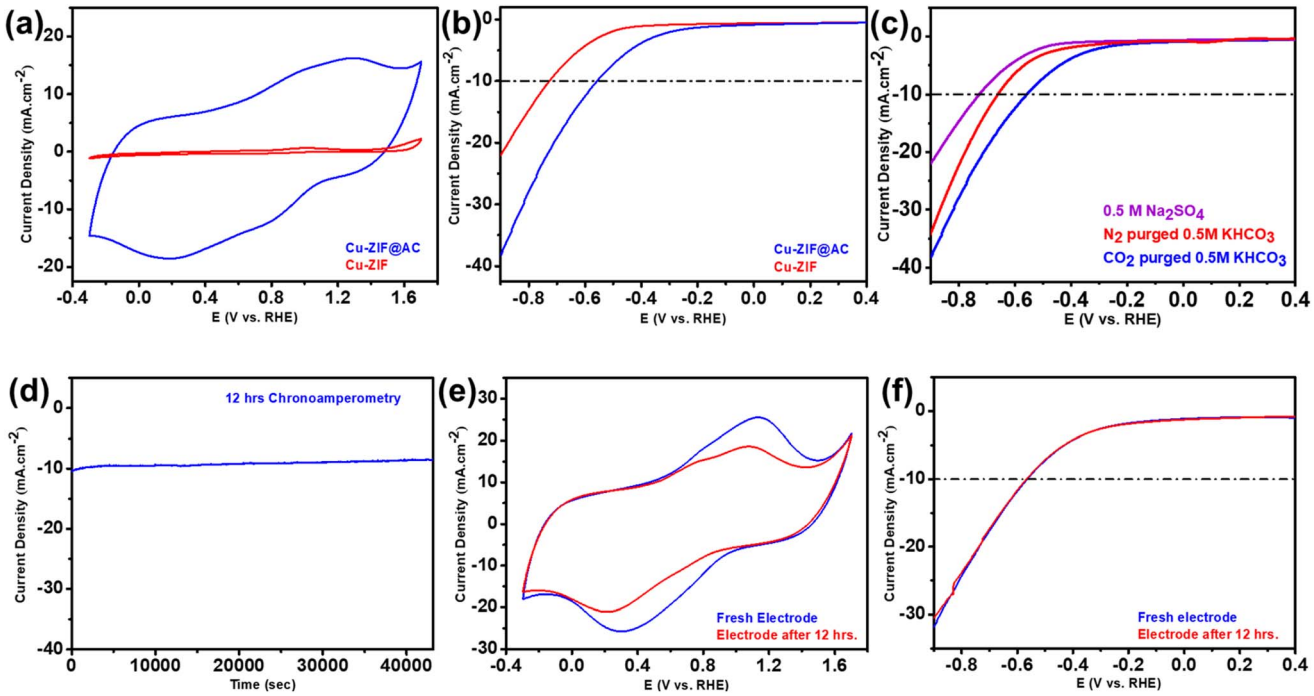

Fig. 3 (a) CV of Cu-ZIF@AC, Cu-ZIF in N_2 saturated 0.5 M Na_2SO_4; (b) LSV of Cu-ZIF@AC, Cu-ZIF in CO_2 saturated 0.5 M $KHCO_3$; (c) LSV of Cu-ZIF@AC in 0.5 M Na_2SO_4, N_2 and CO_2 saturated 0.5 M $KHCO_3$; (d) 12 h of stability test using chronoamperometry for Cu-ZIF@AC in CO_2 saturated 0.5 M $KHCO_3$ at constant potential of −0.56 V *vs.* RHE; (e) CV of Cu-ZIF@AC coated fresh electrode and electrode after 12 h of chronoamperometry; (f) LSV of Cu-ZIF@AC coated fresh electrode and electrode after 12 h of chronoamperometry.

measurements were performed (Table S2). The Nyquist plots (Fig. S4) show that the charge-transfer resistance (R_{ct1}) of pristine Cu-ZIF is significantly high (133.98 Ω), confirming its intrinsically poor electrical conductivity. In contrast, Cu-ZIF@AC exhibits a dramatically reduced R_{ct1} value (4.89 Ω), which is slightly more than that of bare AC (3.91 Ω). This substantial decrease in R_{ct1} clearly demonstrates that incorporating Cu-ZIF within the conductive AC matrix greatly enhances interfacial electron transfer kinetics. The reduced charge-transfer resistance provides direct quantitative evidence supporting the improved conductivity and confirms the synergistic interaction between AC and Cu-ZIF in facilitating efficient electron transport.

During the CO_2RR, the gaseous CO_2 interacted with water to produce carbonic acid (H_2CO_3), facilitating the dissolution of additional CO_2. The formed H_2CO_3 existed in equilibrium with bicarbonate (HCO_3^-), which was further in equilibrium with carbonate (CO_3^{2-}). Under neutral pH conditions, carbonate ions were protonated to yield bicarbonate. Consequently, the CO_2-saturated solution contained a higher concentration of bicarbonate ions participating in the CO_2 reduction reaction.[27]

Linear sweep voltammetry (LSV) was performed for all electrodes at 10 mV s^{-1} scan rate in CO_2-purged 0.5 M $KHCO_3$ to study the electrocatalytic performance for electrochemical CO_2RR. The Cu-ZIF@AC demonstrated an overpotential of −0.56 V *vs.* RHE at −10 mA cm^{-2}, compared to −0.72 V *vs.* RHE for Cu-ZIF, having a lower current density than Cu-ZIF@AC (Fig. 3b). Cu-ZIF@AC composite exhibits the lowest overpotential for CO_2RR at −10 mA cm^{-2} current density among the MOF-based catalysts listed in Table S1.[27,47–57] The results demonstrate that the growth of MOF within the pores of activated carbon enhances the catalytic activity of the composite towards CO_2RR. Considering the limited solubility and diffusion coefficient of CO_2 in aqueous electrolytes, partial mass transport limitations may arise in H-cell configurations at higher overpotentials. To minimize concentration polarization, the electrolyte was continuously stirred during electrolysis, and the catalyst loading was optimized to avoid excessive catalyst-layer thickness. Therefore, the observed current densities are mainly attributed to catalytic kinetics within the investigated potential range, although some diffusion limitations at more negative potentials cannot be completely excluded.[58,59] To confirm that the cathodic current resulted from CO_2 reduction rather than from the hydrogen evolution reaction (HER, $2H^+ + 2e^- \rightarrow H_2$), the LSV was re-performed using a N_2-saturated 0.5 M $KHCO_3$ electrolyte at 10 mV s^{-1} scan rate. In this CO_2-free environment, the overpotential shifted to −0.66 V *vs.* RHE at −10 mA cm^{-2} (Fig. 3c), indicating that the reduction process was dominated by HER, thereby confirming the catalyst's strong selectivity for CO_2 reduction. LSV measurements were also performed in 5 M Na_2SO_4, a CO_2-free, non-carbonate electrolyte, to evaluate the intrinsic HER activity of the Cu-ZIF@AC under inert conditions exhibiting overpotential of to −0.72 V *vs.* RHE at −10 mA cm^{-2}.

The stability of the electrode is one of the challenges in electrocatalysis. To examine the stability of Cu-ZIF@AC electrode, chronoamperometry was performed at −0.56 V *vs.* RHE for 12 h in CO_2-saturated 0.5 M $KHCO_3$ solution, showing an

average current density of −10 mA cm^{-2} (Fig. 3d). Cu-ZIF@AC shows more electrochemical stability than AC and Cu-ZIF (Fig. S3) indicates that the growth of nano-Cu-ZIF inside the activated carbon pores improves electrochemical stability of the composite over 12 h of chronoamperometry. The redox peak in the CV of the Cu-ZIF@AC coated electrode after 12 hours of chronoamperometry was slightly shifted from that of the fresh electrode (Fig. 3e). The LSV of the electrode after 12 hours of chronoamperometry almost overlapped with that of the fresh electrode, indicating the durability of the electrode is good enough (Fig. 3f).

To further understand catalyst durability, PXRD analysis (Fig. S7b) of the catalyst before and after 12 h electrolysis was carried out. The diffraction peak intensity decreases and slightly shifted after prolonged electrolysis, suggesting partial structural modification and a decrease in crystallinity. This behaviour may be associated with catalyst surface reconstruction, partial loss of active sites, or adsorption of reaction intermediates, products on the catalyst surface during extended electrolysis, potentially contributing to catalyst deactivation.

3.3 Product analysis

The CO_2RR products were analysed using a 400 MHz NMR and quantified using eqn (5) at different potentials. The NMR diagrams of observed products at different potentials and different times are shown in (Fig. S5 and S6). The F.E. (%) describes the fraction of total charge contributed to the formation of each product. The F.E. (%) was calculated using eqn (6) at different potentials and also at −0.3 V for different times of product collection.

The faradaic efficiency profile, shown in Fig. 4a, exhibits a clear potential-dependent distribution of products. Across all applied potentials, acetic acid (AcOH) remains the predominant product, contributing the largest fraction of F.E. At −0.3 V potential, the highest F.E. of 71.5 ± 0.29% is found for AcOH outperforming several previously reported MOF- and Cu-based catalysts summarized in Table S1.[55–57] As potential becomes more negative, the F.E. of AcOH gradually decreases 54.79 ± 0.15%, 49.8 ± 0.12, 44.23 ± 0.15%, 27.53 ± 0.17%, 19.12 ± 0.14% at −0.4, −0.5, −0.56, −0.6, −0.7 V (*vs.* RHE) respectively accompanied by a concurrent rise in competitive Hydrogen Evolution Reaction (HER). Minor amounts of formic acid (HCOOH) and methanol (MeOH) were detected. Overall, the plot demonstrates that the catalytic system primarily favours AcOH formation at low potential. But, decrease in C_2 product faradaic efficiency was observed with increasing negative potentials. While C_2 formation on Cu-based catalysts is generally favored within an optimal potential window, deviations from this trend can occur due to changes in reaction kinetics and competing hydrogen evolution reaction (HER). In the present system, the enhanced HER at higher cathodic potentials competes for active sites and protons, thereby limiting the availability of CO_2 reduction intermediates required for C–C coupling. As a result, the selectivity shifts away from C_2 products at more negative potentials, indicating a competition-controlled regime between CO_2 reduction and HER rather than a monotonic potential dependence.[60,61]

At an onset potential of −0.3 V (*vs.* RHE), the F.E. profile (Fig. 4b) demonstrates that acetic acid (AcOH) is the predominant CO_2RR product over 15–60 minutes of chronoamperometry in CO_2-purged 0.5 M $KHCO_3$. Minor formation of HCOOH, MeOH, and H_2 was observed. The consistent product distribution over time confirms the catalyst's stable activity and sustained selectivity towards AcOH at an onset potential of −0.3 V (*vs.* RHE).

To further confirm the stability of product selectivity during long-term operation, gas chromatography (GC) calibration was performed for quantitative determination of acetic acid, and the faradaic efficiency (F.E.) was evaluated at different time intervals during the 12 h chronoamperometric test at −0.56 V *vs.* RHE maintaining −10 mA cm^{-2} current density. The GC calibration curve and the corresponding time-dependent F.E. results are provided in Fig. S7. The F.E. toward acetic acid remains relatively stable throughout the electrolysis period, indicating that the Cu-ZIF@AC electrode maintains both activity and selectivity under extended electrochemical operation.

Gas-phase FTIR (Fig. S8) did not detect CO in the product stream, suggesting that although the reaction may proceed through a CO-mediated pathway, any transiently formed CO is rapidly consumed and further reduced to downstream products on the Cu-ZIF@AC catalyst. To detect gas phase product like CH_4, C_2H_4, we performed Mass Spectroscopy of the samples taken from mouth space of the H-cell cathode chamber but no gas phase product was detected except H_2 gas.

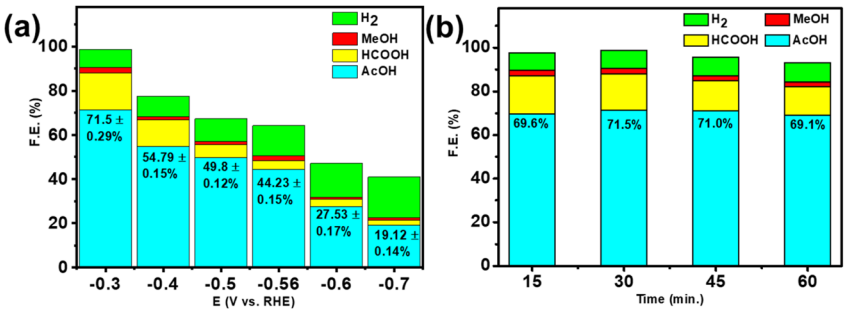

Fig. 4 (a) Faradaic efficiency with error bar of the CO_2RR products at different potentials (*vs.* RHE) of chronoamperometry; (b) faradaic efficiency of CO_2RR products at −0.3 V *vs.* RHE onset potential at different times of chronoamperometry.

3.4 Structural and geometrical optimization of Cu-ZIF

To clarify the relationship between catalytic activity and structural sites, the Cu-ZIF framework was modulated and analysed using DFT calculations. These calculations were used to identify the most active Cu sites for CO_2 activation and their conversion to CH_3COOH within the Cu-MOF. We relaxed the Cu-ZIF structures without any symmetric constraints for the structural and geometrical optimization.

Fig. 5 depicts the optimized primitive cell of the Cu-ZIF. The optimized unit cell of the Cu-ZIF contains 276 atoms, with lattice parameters: $a = 16.33$ Å, $b = 16.61$ Å, $c = 16.62$ Å, and angles $\alpha = 93.00°$, $\beta = 106.61°$, $\gamma = 100.06°$. The Cu–N bond lengths range from 1.96 Å to 2.03 Å. Each copper atom is tetrahedrally coordinated to the nitrogen atoms of the ligands, exhibiting two distinct bond lengths. This variation may arise from the unsymmetrically filled t_{2g} orbitals of Cu^{2+} (d^9 configuration),[62,63] as well as steric repulsions from the methyl groups or other framework atoms.[64,65] The unit cell is constructed from a combination of six distorted four-membered rings and eight six-membered rings, forming the three-dimensional Cu-ZIF framework.

To further investigate the electronic structure of the Cu active sites, additional spin-polarized calculations were performed using different magnetic initializations. The spin-polarized configuration initialized with MAGMOM = 0.6 converged to the lowest-energy state with a total energy of −1756.0987 eV, whereas the non-spin-polarized configuration (ISPIN = 1) exhibited a higher energy of −1755.5236 eV. The stabilization energy of approximately 0.64 eV demonstrates that the Cu-ZIF framework energetically favours a spin-polarized electronic ground state.

The origin of this stabilization is associated with the distorted tetrahedral coordination environment surrounding the Cu centers. In Cu^{2+} ($3d^9$), the ligand-field splitting generated by the tetrahedrally distorted Cu–N coordination is insufficient to fully quench the unpaired Cu 3d electron density, thereby preserving localized magnetic moments at the Cu sites. Such spin-polarized Cu d states can significantly influence the adsorption and activation of CO_2 molecules through enhanced electronic coupling and orbital hybridization between the Cu centres and adsorbate frontier orbitals. Consequently, the local coordination geometry and magnetic electronic structure collectively contribute to the catalytic behaviour of the Cu-ZIF framework.

3.5 Thermodynamic energy analysis for Cu-ZIF and catalytic pathway

Due to its asymmetrical chemical environment, the Cu-based zeolitic imidazole framework (Cu-ZIF) contains twelve distinct Cu sites available for CO_2 adsorption. To investigate variations in the catalytic behaviour of these sites, a single CO_2 molecule was adsorbed onto each of the twelve Cu centres. The corresponding adsorption energies were calculated using eqn (7) and are summarized in Tables S3 to S6. Among these, the most stable, least stable, and intermediate stable adsorption configurations, denoted as Cu_3, Cu_7, and Cu_5, with adsorption energies of −0.58 eV, −0.18 eV, and −0.36 eV, respectively, were selected for detailed analysis. As illustrated in Fig. 5b and c, CO_2 molecules are preferentially adsorbed within the 4 or 6-membered pores of the ZIF. Probably one of the oxygen atoms of CO_2 interacts strongly with the Cu centre, resulting in a slight elongation of one C–O bond.[66] The adsorption energy values,

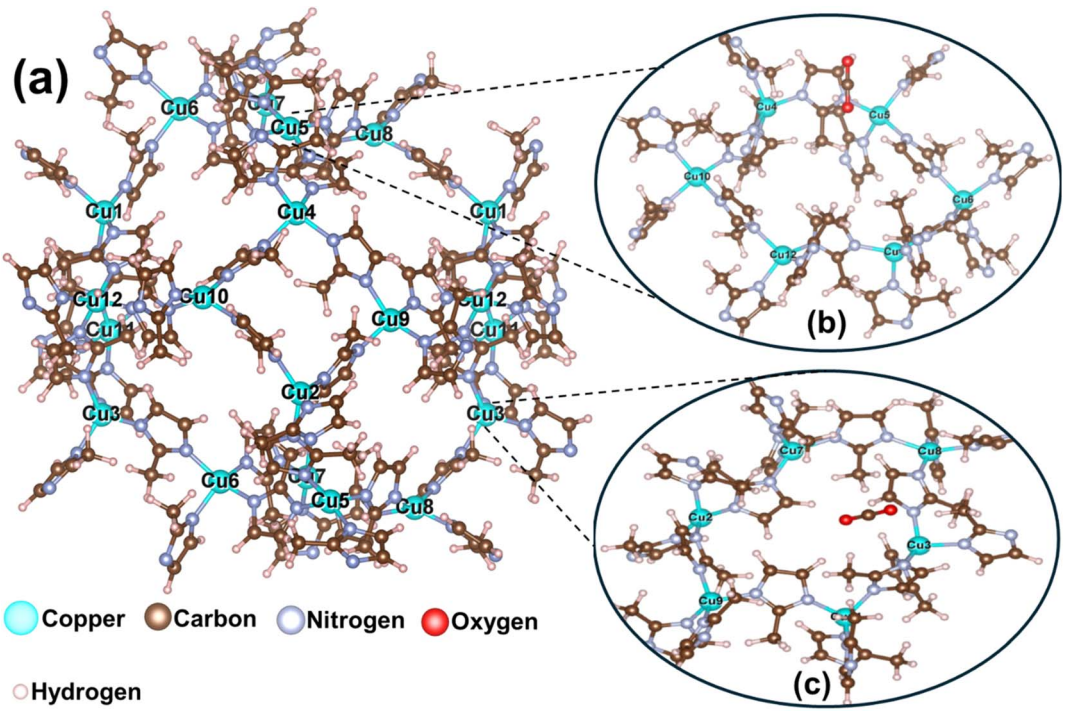

Fig. 5 (a) Structural and geometrical optimized bulk system of Cu-ZIF; CO_2 adsorbed at (b) Cu_5 and (c) Cu_3 sites of Cu-ZIF.

together with the molecular orientation of CO_2 within the pores, reveal the contributions of van der Waals and electrostatic interactions to the overall binding strength.

The catalytic behaviour of the Cu adsorption sites is also influenced by the spin-polarized electronic structure of the Cu-ZIF framework. The distorted tetrahedral coordination around the Cu centers preserves partially occupied Cu 3d states, resulting in localized magnetic character at the active sites. Such spin polarization modifies the electronic interaction between the Cu centers and adsorbed CO_2-derived intermediates, including *OCHO and *COOH.

The variation in adsorption energies among the Cu_3, Cu_5, and Cu_7 sites therefore arises not only from differences in local geometric confinement within the framework pores but also from differences in the electronic structure of the individual Cu centers. In particular, the stronger stabilization observed at the Cu_3 site is attributed to favourable orbital interactions between the spin-polarized Cu d states and the adsorbate orbitals, leading to enhanced stabilization of the *OCHO intermediate. In contrast, the comparatively weaker adsorption at Cu_7 alters the relative stability of the *COOH intermediate and promotes a competing reaction pathway. These results demonstrate that the interplay between distorted coordination geometry and spin-polarized electronic structure plays an important role in governing the site-dependent CO_2 electroreduction mechanism in Cu-ZIF.

During the initial proton–electron transfer in CO_2 electroreduction, two competing intermediates (*OCOH and *COOH) may form depending on the protonation site.[67] The distinct coordination environments of the Cu_n ($n = 3, 5, 7$) active sites result in variations in intermediate stabilization and reaction pathways toward CH_3COOH, as shown in Fig. 6a.

Comparative energetics reveals that Cu_3 favours the *OCHO-mediated pathway, as *OCHO formation 1.59 eV and its subsequent hydrogenation proceed with the lowest energy penalties (*vs.* 2.09 eV for COOH). The hydrogenation of *OCHO to *OCHOH proceeds thermodynamically favourably with a reaction energy of −1.61 eV, whereas the subsequent conversion of *OCHOH to *CHO requires a substantial energy input, 1.88 eV, associated with C–O bond cleavage, identifying it as a key uphill step in the reaction pathway. The following hydrogenation steps from *CHO to *CHOH and then to *CH_2OH occur readily, facilitating further reduction of the intermediate. However, the formation of *CH_2 from *CH_2OH involves an additional energetic penalty (1.40 eV). Once *CH_2 is generated, subsequent hydrogenation to *CH_3 and ultimately to CH_3COOH becomes strongly exergonic (−2.41 eV and −1.00 eV, respectively), driving the reaction toward the formation of a stable CH_3COOH product as shown in Fig. 6a. Cu_5 also follows a predominantly OCHO-based mechanism, with subsequent hydrogenation to OCHOH, which is an exergonic step with a free energy change of −1.63 eV. The transformation of *OCHOH to *CHO constitutes a key thermodynamically demanding step in the *OCHO-mediated pathway of 1.77 eV. Subsequent hydrogenation to *CH_2O proceeds favourably, while further reduction to *CH_2OH and its conversion to *CH_2 involves an energetic penalty of 2.36 eV. Notably, once *CH_2 is formed, the remaining hydrogenation steps toward *CH_3 and ultimately CH_3COOH are strongly downhill in energy (−2.51 eV and −2.00 eV, respectively). Overall, these energetic trends demonstrate that the OCHO route is thermodynamically well-aligned for efficient CH_3COOH formation. Nonetheless, strong exergonicity in the final hydrogenation steps still promotes CH_3COOH formation.

In contrast to the Cu_3 and Cu_5 sites, the Cu_7 site (Fig. 6a) supports a competing *COOH-mediated reaction pathway, in which *COOH step of 0.24 eV is thermodynamically more stable than *OCHO step of 1.34 eV, indicating a preference for this intermediate. The conversion of *COOH to *CO involves only a modest energetic requirement of 0.28 eV, after which hydrogenation of *CO proceeds preferentially *via* the *CHO (1.45 eV) intermediate rather than *COH (1.67 eV). Subsequent hydrogenation steps from *CHO to *CH_2O is largely favourable and further to *CH_2OH step at a low energy cost of −1.73 eV and 0.36 eV, respectively, enabling smooth progression along the pathway. However, C–O bond cleavage during the transformation of *CH_2OH to *CH_2 is a highly energetically demanding step of 2.53 eV at the Cu_7 site, representing a significant bottleneck. Once this barrier is overcome, the remaining hydrogenation steps toward *CH_3 and ultimately CH_3COOH are strongly exergonic (−2.57 eV and −1.97 eV, respectively), thereby favouring the formation of acetic acid despite the presence of an energetically challenging intermediate step.

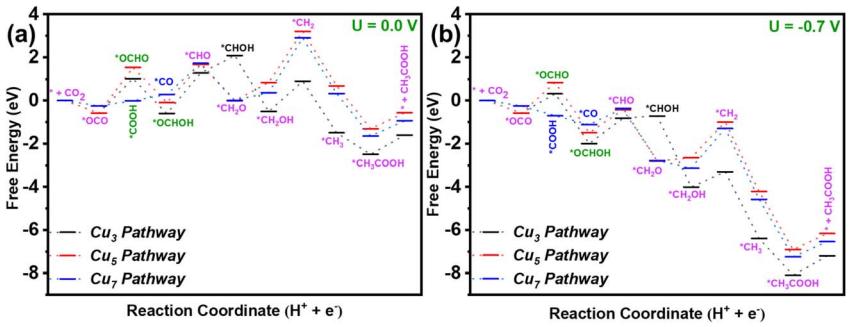

Fig. 6 Free energy profile for CO_2 to CH_3COOH on Cu-ZIF at Cu_3, Cu_5, Cu_7 sites (a) 0.0 V *vs.* RHE and (b) −0.7 V *vs.* RHE. Black, red, blue legends represent the CH_3COOH pathway for Cu_3, Cu_5, Cu_7 copper adsorbing sites in the Cu-ZIF, respectively.

Under an applied potential of −0.7 V *vs.* RHE (maximum potential applied experimentally), the free energies of most intermediates become negative, indicating spontaneous progression toward CH_3COOH on all three catalysts. Even with this potential shift, Cu_3 maintains the lowest overall thermodynamic reaction energy (−1.45 eV) without any applied potential for CO_2 to CH_3COOH, demonstrating superior catalytic activity relative to Cu_5 (−1.05) and Cu_7 (−1.41 eV) (Fig. 6b). At an applied experimental potential of −0.70 V *vs.* RHE, the calculated thermodynamic reaction energies for the Cu_3, Cu_5, and Cu_7 sites are −7.05, −6.65, and −7.01 eV, respectively. Similarly, at other experimental applied potentials of −0.56 and −0.30 V was also performed as shown in Fig. S11 and the corresponding reaction energies for Cu_3, Cu_5, Cu_7 are −5.93, −5.53, −5.89 eV and −3.85, −3.45, −3.81 eV, respectively.

The asymmetric Cu-ZIF offers multiple Cu active sites with distinct CO_2 adsorption strengths and reaction energetics, resulting in site-dependent CO_2 electroreduction pathways. Among the investigated sites, Cu_3 and Cu_5 preferentially promote the *OCHO-mediated route, while Cu_7 favours a competing *COOH pathway. In all cases, C–O bond cleavage from *OCHOH or $*CH_2OH$ to $*CH_2$ constitutes the key thermodynamic bottleneck, whereas the final hydrogenation steps toward CH_3COOH are strongly exergonic. Overall, Cu_3 exhibits the most favourable adsorption and lowest overall reaction free energy, identifying it as the most active site for acetic acid formation.

4 Conclusions

This work demonstrates the high electrocatalytic efficiency of a composite material consisting of the Cu-ZIF integrated with activated carbon for CO_2 electroreduction. Because MOFs are inherently insulating, establishing electrical conductivity is a prerequisite for their application in electrochemical systems. In this study, Cu-ZIF nanoparticles were grown inside a conductive porous carbon matrix. Notably, X-ray diffraction confirmed that incorporation into the carbon support did not alter the crystalline structure of Cu-ZIF. When tested in CO_2-saturated aqueous electrolyte, the composite electrode exhibited excellent catalytic activity, with an onset potential of −0.3 V *vs.* RHE and a current density of $-10\ mA\ cm^{-2}$ at −0.56 V. The composite also demonstrated strong operational stability, maintaining nearly constant performance over 12 hours of continuous electrolysis. ^{1}H-NMR analysis identified acetic acid as the primary reduction product. Collectively, these findings highlight the effectiveness of this composite design by growing nano-Cu-ZIF in activated carbon, thereby enabling Cu-ZIF's efficient participation in electrochemical CO_2 reduction.

Conflicts of interest

There are no conflicts to declare.

Data availability

All data supporting this study are provided within the article and supplementary information (SI). Raw electrochemical data, NMR spectra, structural characterization files, and density functional theory (DFT) input/output files are available from the corresponding author upon reasonable request. Supplementary information is available. See DOI: https://doi.org/10.1039/d6na00256k.

Acknowledgements

The authors thank the Israel National Institute for Energy Storage (INIES) for supporting this research. The ministry of science and technology under grant #8127.

References

1 F. N. Al-Rowaili, A. Jamal, M. S. Ba Shammakh and A. Rana, A Review on Recent Advances for Electrochemical Reduction of Carbon Dioxide to Methanol Using Metal-Organic Framework (MOF) and Non-MOF Catalysts: Challenges and Future Prospects, *ACS Sustain. Chem. Eng.*, 2018, **6**(12), 15895–15914.
2 I. V. Moroz, A. P. Ekonomov, J. F. Kasting, T. P. Ackerman and C. M. Pieters, Climating Consequences of Very High Carbon Dioxide Levels in the Earth's Early Atmosphere, *Science*, 1986, **234**(4782), 1383–1385.
3 H. Wang, B. W. Ang and B. Su, A Multi-Region Structural Decomposition Analysis of Global CO2 Emission Intensity, *Ecol. Econ.*, 2017, **142**, 163–176.
4 Y. Y. Birdja, E. Pérez-Gallent, M. C. Figueiredo, A. J. Göttle, F. Calle-Vallejo and M. T. M. Koper, Advances and Challenges in Understanding the Electrocatalytic Conversion of Carbon Dioxide to Fuels, *Nat. Energy*, 2019, 732–745.
5 C. W. Li and M. W. Kanan, CO 2 Reduction at Low Overpotential on Cu Electrodes Resulting from the Reduction of Thick Cu 2O Films, *J. Am. Chem. Soc.*, 2012, **134**(17), 7231–7234.
6 C. Reller, R. Krause, E. Volkova, B. Schmid, S. Neubauer, A. Rucki, M. Schuster and G. Schmid, Selective Electroreduction of CO2 toward Ethylene on Nano Dendritic Copper Catalysts at High Current Density, *Adv. Energy Mater.*, 2017, **7**(12), 1602114.
7 D. Ren, Y. Deng, A. D. Handoko, C. S. Chen, S. Malkhandi and B. S. Yeo, Selective Electrochemical Reduction of Carbon Dioxide to Ethylene and Ethanol on Copper(I) Oxide Catalysts, *ACS Catal.*, 2015, **5**(5), 2814–2821.
8 M. K. Yadav, A. Dutta, A. Lal, H. Porat, T. Zidki and A. Borenstein, Laser-Induced Synthesis of Copper-Based Nanomaterials for CO2Electroreduction into Methanol, *ACS Appl. Energy Mater.*, 2025, **8**(17), 12641–12650.
9 R. M. Arán-Ais, D. Gao and B. Roldan Cuenya, Structure- and Electrolyte-Sensitivity in CO2 Electroreduction, *Acc. Chem. Res.*, 2018, **51**(11), 2906–2917.
10 R. Kortlever, J. Shen, K. J. P. Schouten, F. Calle-Vallejo and M. T. M. Koper, Catalysts and Reaction Pathways for the Electrochemical Reduction of Carbon Dioxide, *J. Phys. Chem. Lett.*, 2015, **6**(20), 4073–4082.
11 P. Shao, H. X. Zhang, Q. L. Hong, L. Yi, Q. H. Li and J. Zhang, Enhancing CO2 Electroreduction to Ethylene *via* Copper–

Silver Tandem Catalyst in Boron-Imidazolate Framework Nanosheet, *Adv. Energy Mater.*, 2023, **13**(19), 2300088.

12 H. Gao, T. Yang, W. Nie, Y. Gao, Z. Wang and A. Dong, Recent Advances in Cu-Based Metal–Organic Framework Electrocatalysts for CO2 Reduction Reactions, *Catalysts*, 2025, 328.

13 Z.-Z. Niu, X.-L. Zhang, L.-P. Chi, Y.-C. Zhang, M.-H. Fan and M.-R. Gao, Revealing the Formation and Impact of Oxygen-Containing Species on Cu Surface during CO 2/CO Electroreduction, *Artif. Photosynth.*, 2026, **2**(3), 154–165.

14 J. W. DuanMu, Z. Z. Wu, F. Y. Gao, P. P. Yang, Z. Z. Niu, Y. C. Zhang, L. P. Chi and M. R. Gao, Investigation and Mitigation of Carbon Deposition over Copper Catalyst during Electrochemical CO2 Reduction, *Precis. Chem.*, 2024, **2**(4), 151–160.

15 Z. Z. Niu, L. P. Chi, Z. Z. Wu, P. P. Yang, M. H. Fan and M. R. Gao, CO2-Assisted Formation of Grain Boundaries for Efficient CO–CO Coupling on a Derived Cu Catalyst, *Natl. Sci. Open*, 2023, **2**(2), 20220044.

16 X. Li, X. Yang, H. Xue, H. Pang and Q. Xu, Metal–Organic Frameworks as a Platform for Clean Energy Applications, *EnergyChem*, 2020, **2**(2), 100027.

17 H. Furukawa, K. E. Cordova, M. O'Keeffe and O. M. Yaghi, The Chemistry and Applications of Metal-Organic Frameworks, *Science*, 2013, **341**(6149), 1230444.

18 A. N. Hong, H. Yang, X. Bu and P. Feng, Pore Space Partition of Metal-Organic Frameworks for Gas Storage and Separation, *EnergyChem*, 2022, **4**(4), 100080.

19 N. Kornienko, Y. Zhao, C. S. Kley, C. Zhu, D. Kim, S. Lin, C. J. Chang, O. M. Yaghi and P. Yang, Metal-Organic Frameworks for Electrocatalytic Reduction of Carbon Dioxide, *J. Am. Chem. Soc.*, 2015, **137**(44), 14129–14135.

20 S. Kusama, T. Saito, H. Hashiba, A. Sakai and S. Yotsuhashi, Crystalline Copper(II) Phthalocyanine Catalysts for Electrochemical Reduction of Carbon Dioxide in Aqueous Media, *ACS Catal.*, 2017, **7**(12), 8382–8385.

21 K. Sathiyan, A. Dutta, V. Marks, O. Fleker, T. Zidki, R. D. Webster and A. Borenstein, Nano-Encapsulation: Overcoming Conductivity Limitations by Growing MOF Nanoparticles in Meso-Porous Carbon Enables High Electrocatalytic Performance, *NPG Asia Mater.*, 2023, **15**(1), 18.

22 V. B. Kumar, A. Borenstein, B. Markovsky, D. Aurbach, A. Gedanken, M. Talianker and Z. Porat, Activated Carbon Modified with Carbon Nanodots as Novel Electrode Material for Supercapacitors, *J. Phys. Chem. C*, 2016, **120**(25), 13406–13413.

23 A. Dutta, S. T. Y. Trolles-Cavalcante, A. Cleetus, V. Marks, A. Schechter, R. D. Webster and A. Borenstein, Surface Modifications of Carbon Nanodots Reveal the Chemical Source of Their Bright Fluorescence, *Nanoscale Adv.*, 2021, **3**(3), 716–724.

24 P. Bhadane, P. Mahato, D. Menon, B. K. Satpathy, L. Wu, S. Chakraborty, P. Goyal, I. Lynch and S. K. Misra, Hydrolytically Stable Nanosheets of Cu–Imidazolate MOF for Selective Trapping and Simultaneous Removal of Multiple Heavy Metal Ions, *Environ. Sci. Nano*, 2024, **11**(6), 2385–2396.

25 E. Elanthamilan, S. Rajkumar, R. Rajavalli and J. P. Merlin, Cost Effective Synthesis of a Copper-1 H-Imidazole@activated Carbon Metal Organic Framework as an Electrode Material for Supercapacitor Applications, *New J. Chem.*, 2018, **42**(12), 10300–10308.

26 S. Duan, L. Wu, J. Li, Y. Huang, X. Tan, T. Wen, T. Hayat, A. Alsaedi and X. Wang, Two-Dimensional Copper-Based Metal–organic Frameworks Nano-Sheets Composites: One-Step Synthesis and Highly Efficient U(VI) Immobilization, *J. Hazard. Mater.*, 2019, **373**, 580–590.

27 K. Sathiyan, A. Dutta, V. Marks, O. Fleker, T. Zidki, R. D. Webster and A. Borenstein, Nano-Encapsulation: Overcoming Conductivity Limitations by Growing MOF Nanoparticles in Meso-Porous Carbon Enables High Electrocatalytic Performance, *NPG Asia Mater.*, 2023, **15**(1), 18.

28 O. Fleker, A. Borenstein, R. Lavi, L. Benisvy, S. Ruthstein and D. Aurbach, Preparation and Properties of Metal Organic Framework/Activated Carbon Composite Materials, *Langmuir*, 2016, **32**(19), 4935–4944.

29 S. Niu, S. Li, Y. Du, X. Han and P. Xu, How to Reliably Report the Overpotential of an Electrocatalyst, *ACS Energy Lett.*, 2020, **5**(4), 1083–1087.

30 X. Jiang, L. Ke, K. Zhao, X. Yan, H. Wang, X. Cao, Y. Liu, L. Li, Y. Sun, Z. Wang, D. Dang and N. Yan, Integrating Hydrogen Utilization in CO2 Electrolysis with Reduced Energy Loss, *Nat. Commun.*, 2024, **15**(1), 1427.

31 C. Li, Y. Ji, Y. Wang, C. Liu, Z. Chen, J. Tang, Y. Hong, X. Li, T. Zheng, Q. Jiang and C. Xia, Applications of Metal–Organic Frameworks and Their Derivatives in Electrochemical CO2 Reduction, *Nano-Micro Lett.*, 2023, **15**(1), 113.

32 J. Hafner, *Ab-initio* Simulations of Materials Using VASP: Density-functional Theory and Beyond, *J. Comput. Chem.*, 2008, **29**(13), 2044–2078.

33 W. Kohn and L. J. Sham, Self-Consistent Equations Including Exchange and Correlation Effects, *Phys. Rev.*, 1965, **140**(4A), A1133–A1138.

34 J. P. Perdew, K. Burke and M. Ernzerhof, Generalized Gradient Approximation Made Simple, *Phys. Rev. Lett.*, 1996, **77**(18), 3865–3868.

35 P. E. Blöchl, Projector Augmented-Wave Method, *Phys. Rev. B: Condens. Matter Mater. Phys.*, 1994, **50**(24), 17953–17979.

36 S. Grimme, Semiempirical GGA-type Density Functional Constructed with a Long-range Dispersion Correction, *J. Comput. Chem.*, 2006, **27**(15), 1787–1799.

37 H. J. Monkhorst and J. D. Pack, Special Points for Brillouin-Zone Integrations, *Phys. Rev. B: Condens. Matter Mater. Phys.*, 1976, **13**(12), 5188–5192.

38 V. Wang, N. Xu, J.-C. Liu, G. Tang and W.-T. Geng, VASPKIT: A User-Friendly Interface Facilitating High-Throughput Computing and Analysis Using VASP Code, *Comput. Phys. Commun.*, 2021, **267**, 108033.

39 L. Zou, P. Shao, K. Zhang, L. Yang, D. You, H. Shi, S. G. Pavlostathis, W. Lai, D. Liang and X. Luo, Tannic Acid-Based Adsorbent with Superior Selectivity for Lead(II)

Capture: Adsorption Site and Selective Mechanism, *Chem. Eng. J.*, 2019, **364**, 160–166.

40 Y. Zhao and D. G. Truhlar, Density Functional Theory for Reaction Energies: Test of Meta and Hybrid Meta Functionals, Range-Separated Functionals, and Other High-Performance Functionals, *J. Chem. Theory Comput.*, 2011, **7**(3), 669–676.

41 D. R. Alfonso, D. N. Tafen and D. R. Kauffmann, First-Principles Modeling in Heterogeneous Electrocatalysis, *Catalysts*, 2018, **8**(10), 424.

42 J. K. Nørskov, F. Studt, F. Abild-Pedersen and T. Bligaard, *Fundamental Concepts in Heterogeneous Catalysis*, Wiley, 2014, DOI: 10.1002/9781118892114.

43 Y. Yu, C. Yue, X. Lin, S. Sun, J. Gu, X. He, C. Zhang, W. Lin, D. Lin, X. Liao, B. Xu, S. Wu, M. Zheng, J. Li, J. Kang and L. Lin, ZIF-8 Cooperating in TiN/Ti/Si Nanorods as Efficient Anodes in Micro-Lithium-Ion-Batteries, *ACS Appl. Mater. Interfaces*, 2016, **8**(6), 3992–3999.

44 J. C. Muñoz-Senmache, S. Kim, R. R. Arrieta-Pérez, C. M. Park, Y. Yoon and A. J. Hernández-Maldonado, Activated Carbon–Metal Organic Framework Composite for the Adsorption of Contaminants of Emerging Concern from Water, *ACS Appl. Nano Mater.*, 2020, **3**(3), 2928–2940.

45 C. Bläker, J. Muthmann, C. Pasel and D. Bathen, Characterization of Activated Carbon Adsorbents – State of the Art and Novel Approaches, *ChemBioEng Rev.*, 2019, **6**(4), 119–138.

46 C. Fan, V. Nguyen, Y. Zeng, P. Phadungbut, T. Horikawa, D. D. Do and D. Nicholson, Novel Approach to the Characterization of the Pore Structure and Surface Chemistry of Porous Carbon with Ar, N2, H2O and CH3OH Adsorption, *Microporous Mesoporous Mater.*, 2015, **209**, 79–89.

47 A. Nambi, A. Chatzitakis, U. Olsbye, J. Hjelm, Y. Zhao and A. Kaiser, Gas-Phase Electrochemical CO2 Reduction on Silver-Copper BTC MOF in a Zero-Gap Membrane Electrode Assembly, *Electrochim. Acta*, 2024, **506**, 144763.

48 L. Jia, K. Wagner, J. Smyth, D. Officer, J. Chen and P. Wagner, Cu-THQ-EFG Composite for Highly Selective Electrochemical CO2 Reduction to Formate at Low Overpotentials, *Polymers*, 2022, **14**(23), 5112.

49 Z. Meng, J. Luo, W. Li and K. A. Mirica, Hierarchical Tuning of the Performance of Electrochemical Carbon Dioxide Reduction Using Conductive Two-Dimensional Metallophthalocyanine Based Metal–Organic Frameworks, *J. Am. Chem. Soc.*, 2020, **142**(52), 21656–21669.

50 H. Xue, H. Zhu, J. Huang, P. Liao and X. Chen, Ultrathin Two-Dimensional Triptycence-Based Metal-Organic Framework for Highly Selective CO2 Electroreduction to CO, *Chin. Chem. Lett.*, 2023, **34**(1), 107134.

51 Z. Xin, Z. Yuan, J. Liu, X. Wang, K. Shen, Y. Chen and Y.-Q. Lan, Cu Cluster Embedded Porous Nanofibers for High-Performance CO2 Electroreduction, *Chin. Chem. Lett.*, 2023, **34**(4), 107458.

52 S. Kusama, T. Saito, H. Hashiba, A. Sakai and S. Yotsuhashi, Crystalline Copper(II) Phthalocyanine Catalysts for Electrochemical Reduction of Carbon Dioxide in Aqueous Media, *ACS Catal.*, 2017, **7**(12), 8382–8385.

53 Y.-L. Qiu, H.-X. Zhong, T.-T. Zhang, W.-B. Xu, P.-P. Su, X.-F. Li and H.-M. Zhang, Selective Electrochemical Reduction of Carbon Dioxide Using Cu Based Metal Organic Framework for CO_2 Capture, *ACS Appl. Mater. Interfaces*, 2018, **10**(3), 2480–2489.

54 I. Hod, M. D. Sampson, P. Deria, C. P. Kubiak, O. K. Farha and J. T. Hupp, Fe-Porphyrin-Based Metal–Organic Framework Films as High-Surface Concentration, Heterogeneous Catalysts for Electrochemical Reduction of CO_2, *ACS Catal.*, 2015, **5**(11), 6302–6309.

55 Q. Zhu, X. Sun, D. Yang, J. Ma, X. Kang, L. Zheng, J. Zhang, Z. Wu and B. Han, Carbon Dioxide Electroreduction to C2 Products over Copper-Cuprous Oxide Derived from Electrosynthesized Copper Complex, *Nat. Commun.*, 2019, **10**(1), 3851.

56 H.-L. Zhu, H.-Y. Chen, Y.-X. Han, Z.-H. Zhao, P.-Q. Liao and X.-M. Chen, A Porous π–π Stacking Framework with Dicopper(I) Sites and Adjacent Proton Relays for Electroreduction of CO_2 to C_{2+} Products, *J. Am. Chem. Soc.*, 2022, **144**(29), 13319–13326.

57 K. Zhang, S. Chen, Y. Ge, X. Zhang, Z. Zhang, C. Ye, G. Pan and L. Hu, CuO/Cu_2O Catalyst with Adjustable Cu(II)/Cu(I) for Selective CO_2 Electroreduction to Acetate, *ACS Appl. Nano Mater.*, 2025, **8**(46), 22285–22294.

58 S. Lu, Y. Wang, H. Xiang, H. Lei, B. B. Xu, L. Xing, E. H. Yu and T. X. Liu, Mass Transfer Effect to Electrochemical Reduction of CO2: Electrode, Electrocatalyst and Electrolyte, *J. Energy Storage*, 2022, **52**, 104764.

59 N. T. Nesbitt, T. Burdyny, H. Simonson, D. Salvatore, D. Bohra, R. Kas and W. A. Smith, Liquid–Solid Boundaries Dominate Activity of CO_2 Reduction on Gas-Diffusion Electrodes, *ACS Catal.*, 2020, **10**(23), 14093–14106.

60 S. Nitopi, E. Bertheussen, S. B. Scott, X. Liu, A. K. Engstfeld, S. Horch, B. Seger, I. E. L. Stephens, K. Chan, C. Hahn, J. K. Nørskov, T. F. Jaramillo and I. Chorkendorff, Progress and Perspectives of Electrochemical CO_2 Reduction on Copper in Aqueous Electrolyte, *Chem. Rev.*, 2019, **119**(12), 7610–7672.

61 D. Ren, J. Fong and B. S. Yeo, The Effects of Currents and Potentials on the Selectivities of Copper toward Carbon Dioxide Electroreduction, *Nat. Commun.*, 2018, **9**(1), 925.

62 F. Rodríguez, Unveiling the Local Structure of Cu^{2+} Ions from d-Orbital Splitting. Application to K_2ZnF_4:Cu^{2+} and $KZnF_3$:Cu^{2+}, *Inorg. Chem.*, 2017, **56**(4), 2029–2036.

63 I. B. Bersuker, Pseudo-Jahn–Teller Effect—A Two-State Paradigm in Formation, Deformation, and Transformation of Molecular Systems and Solids, *Chem. Rev.*, 2013, **113**(3), 1351–1390.

64 Z. Wu, D.-C. Sun, J. Liu, C.-L. Tang, T.-L. Deng, X.-Y. Luo and C.-C. Ding, A Theoretical Study of Structure Properties and Stability in Different Ligands Coordinated Cu-MOFs, *Mater. Chem. Phys.*, 2023, **298**, 127401.

65 J. Pang, S. Yuan, J. Qin, C. Liu, C. Lollar, M. Wu, D. Yuan, H.-C. Zhou and M. Hong, Control the Structure of Zr-

Tetracarboxylate Frameworks through Steric Tuning, *J. Am. Chem. Soc.*, 2017, **139**(46), 16939–16945.

66 Z. Cheng, B. J. Sherman and C. S. Lo, Carbon Dioxide Activation and Dissociation on Ceria (110): A Density Functional Theory Study, *J. Chem. Phys.*, 2013, **138**(1).

67 A. Vasileff, X. Zhi, C. Xu, L. Ge, Y. Jiao, Y. Zheng and S.-Z. Qiao, Selectivity Control for Electrochemical CO_2 Reduction by Charge Redistribution on the Surface of Copper Alloys, *ACS Catal.*, 2019, **9**(10), 9411–9417.